Volume 151
Number 6
16 March 2026
Pages 1509-1810

Analyst

rsc.li/analyst

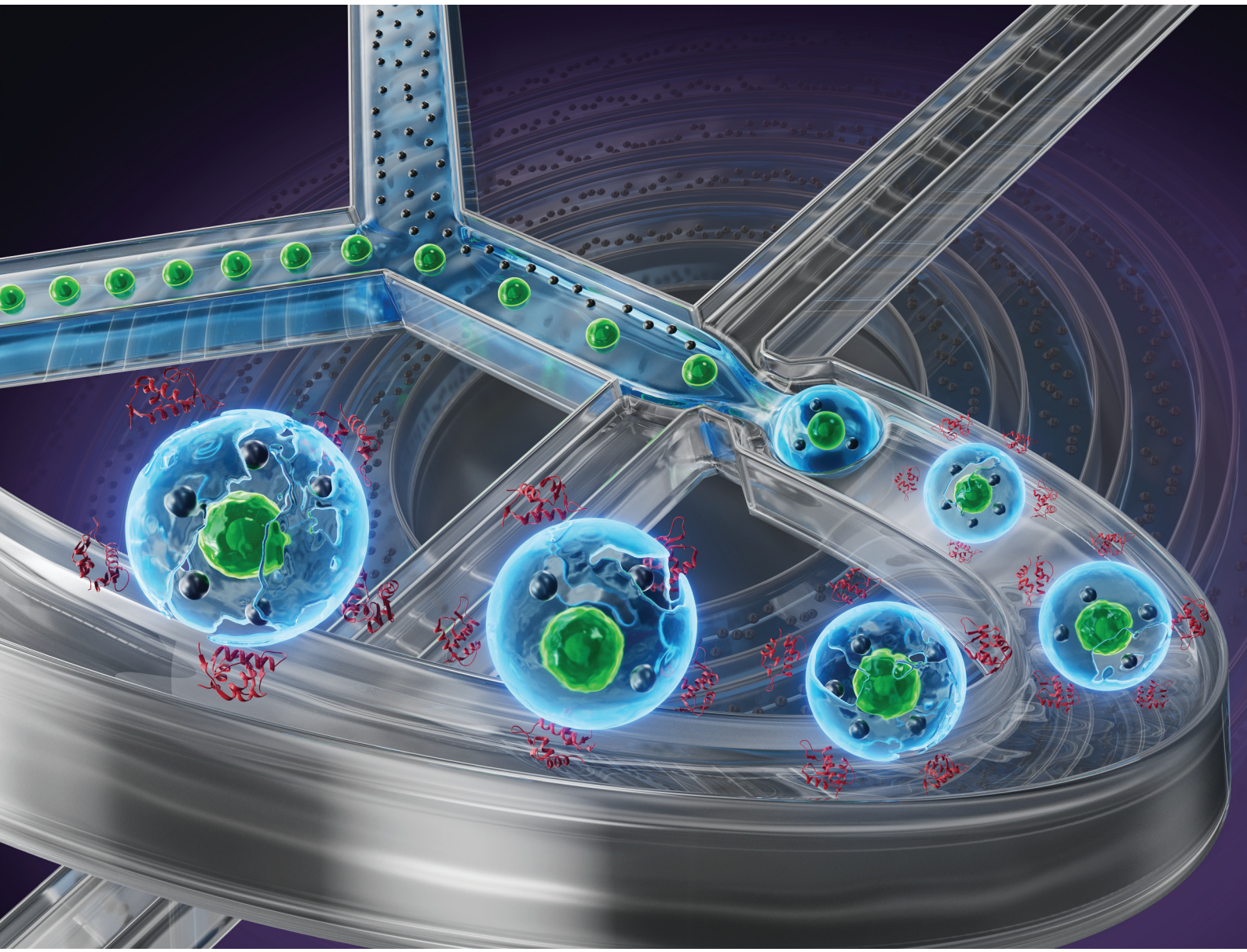

ISSN 0003-2654

ROYAL SOCIETY OF CHEMISTRY

PAPER
Byeong-Ui Moon, Lidija Malic *et al.*
Deterministic droplet-based co-encapsulation of single cells through inertial and hydrodynamic focusing

Analyst

PAPER

View Article Online
View Journal | View Issue

Cite this: *Analyst*, 2026, **151**, 1627

Deterministic droplet-based co-encapsulation of single cells through inertial and hydrodynamic focusing

Byeong-Ui Moon, *[a] Lidija Malic, *[a] Dillon Da Fonte,[a] Liviu Clime,[a] Félix Lussier,[a,b] Ljuboje Lukic,[a] David Juncker[b] and Teodor Veres[a]

Microfluidic techniques for high-throughput encapsulation are powerful tools in single-cell analytics and cytokine profiling. Inertial focusing microfluidics is widely used to align particles in uniform sequences, enhancing encapsulation efficiency. However, on-chip sample dilution strategies to further optimize efficiency remain largely unexplored in deterministic encapsulation approaches, both experimentally and through theoretical modeling. Here, we present a high-yield microparticle encapsulation method that combines inertial and hydrodynamic focusing to enable precise tuning of microparticle spacing and modulation of capture efficiency, thereby offering enhanced operational flexibility for controlled particle encapsulation. We first investigate the microparticle self-ordering behavior within the spiral loop and characterize both flow dynamics and droplet formation regimes. By varying the sheath-to-sample flow rate ratio from 0 to 2, we observe that higher ratios increase the interparticle spacing and shift particles closer to the channel wall. These trends align with both analytical modeling and 3D numerical simulations. Notably, at higher sheath flow ratios (*e.g.*, 1 and 2), single-particle encapsulation exceeds 76%, significantly surpassing Poisson distribution predictions. Moreover, single-cell capture efficiency exceeds 60% under these conditions. In co-encapsulation experiments, we achieved a one-cell-multiple-beads co-encapsulation efficiency near 40%, marking a significant improvement over the Poisson limit. For single-cell applications, we performed co-encapsulation of THP-1 monocytes and streptavidin-coated magnetic beads for TNF-α cytokine detection following lipopolysaccharide stimulation. Cytokine secretion was successfully detected at the single-cell level in both aqueous droplets and alginate hydrogels. We anticipate that this method will offer a promising platform for probing cell–cell interactions and immune responses at single-cell resolution.

Received 15th September 2025,
Accepted 30th January 2026

DOI: 10.1039/d5an00986c

rsc.li/analyst

Introduction

Single-cell analysis enables the study of individually isolated cells by revealing the inherent heterogeneity and individual cellular characteristics that have limitations in traditional bulk cell population analyses.[1] Advanced analytical techniques for single-cell assays are essential for functional assessments, enabling the evaluation of cellular specificity and functionality at the individual cell level. Microfluidically-generated, high-throughput and high-efficiency encapsulation is a promising tool for single cell assays.[2,3] Typically, cell encapsulation is performed using flow focusing geometries to generate water droplets in a continuous oil phase.[4–6] Subsequently, the encapsulated cells are analyzed to detect the presence of cytokines using flow cytometry[7] bead-based immunoassays[2] or indexing droplets.[8]

To improve the encapsulation efficiency, inertial focusing effects[9] of self-ordering are often used to confine and order particles into strings of equally spaced objects.[10] Implementation of inertial focusing effects in a microfluidic channel allows the formation of self-ordered trains of suspended microparticles, which can then be encapsulated using flow-focusing droplet generation junctions. Thus, the periodically positioned microparticles arriving at a constant frequency to the encapsulation junction overcome the stochastic encapsulation limit which is governed by the Poisson distribution. This effectively reduces the number of empty as well as multi-particle droplets. However, to minimize the events encapsulating more than one single cell, most approaches rely on highly diluted suspensions prior to encapsulation with cell concentrations λ (the number of objects in a droplet) ≤ 0.1.[4,11]

[a]*National Research Council of Canada, 75 de Mortagne, Boucherville, Quebec, J4B 6Y4, Canada. E-mail: Ben.Moon@nrc-cnrc.gc.ca, lidija.malic@cnrc-nrc.gc.ca*
[b]*Biomedical Engineering Department, McGill University, 740 Dr Penfield Avenue, Montreal, Quebec, H3A 0G1, Canada*

The resulting emulsion comprises mostly empty droplets with only a small fraction, less than 20%, containing encapsulated cells.[12] When the presence of multiple cells in droplets is considered insignificant for the experimental design, a trade-off is achieved with $\lambda < 0.3$.[13] Nevertheless, the theoretical probability that a droplet contains only one cell (when $\lambda = 1$) is maximized at 36.8%.

To date, both active and passive microfluidic methods have been reported in the literature aiming to overcome the Poisson stochastic encapsulation limit. The active techniques for instance rely on electric actuation,[14,15] magnetic manipulation,[16] surface acoustic wave[17,18] and sorting electrodes.[19,20] In general, these methods provide precise control over encapsulation process, delivering versatile tools for a variety of applications for sorting and manipulation. However, the active approach requires external energy to actuate the objects and often involves complex system configurations and integration of costly additional components. Conversely, the passive encapsulation relies on relatively simpler setups that are more accessible due to the ease of implementation. By simply adapting the microfluidic design and the flow conditions, various encapsulation techniques have been achieved using Dean flows,[10,21] centrifugal fields,[22] viscoelastic fluids,[23] hydrodynamic draining,[13] cell-triggered splitting[24] and resistance-based sample enrichment module.[25] In comparison to active encapsulation, the passive method offers orders of magnitude higher encapsulation efficiency. Nonetheless, the effectiveness of these passive methods relies heavily on the flow rates and fluidic properties that require applying inertial force to the objects.[10,26] A relatively high cell loading density ($\lambda > 1$) combined with fixed flow rates makes it challenging to control single- and multi-object encapsulation. While two-inlet spiral co-encapsulation designs have demonstrated potential,[21,26] comprehensive optimization and parametric studies are still lacking. To address this gap, we propose an alternative approach based on hydrodynamically focused on-chip sample handling. This strategy remains largely unexplored both experimentally and theoretically, particularly in the context of using of combined inertial and hydrodynamic focusing to regulate the λ value (see SI Table S1 for a comparative study of the passive encapsulation strategies).

In this paper, an on-chip concentration-controlled encapsulation method is presented allowing precise control over the interparticle distance through sheath inlet flow, followed by encapsulation in a continuous oil phase with a flow focusing microfluidic junction. We suspended dense microparticles in the dispersed phase inlet and introduced them into the spiral channel to produce microparticle self-ordering under the inertial focusing flow regime. Upon encountering pinching at the first junction, highly concentrated microparticles underwent redistribution by the sheath flow and were subsequently encapsulated in water-in-oil droplets. We systematically studied the effect of the microparticle ordering in sheath flow and used COMSOL numerical simulations as well as 2D analytical modeling to corroborate our findings. The encapsulation efficiency in droplets was also compared with Poisson statistics. In addition, we demonstrated the microparticle co-encapsulation capability of this approach, illustrating its potential for applications requiring co-encapsulation of the cells. Finally, we showed the utility of our system for single-cell level cytokine detection. Here we co-encapsulated THP-1 cells and magnetic assay beads as cytokine detection indicators. Through the chemical stimulation process, we examined the presence of TNF-α in aqueous droplets as well as alginate hydrogels.

Experimental section

Device design and fabrication

The microfluidic device comprises two inlet spiral channels for the aqueous phase, one inlet for oil phase and one outlet. The spiral channel has five loops with a total length of 82 mm (Fig. 1a). The width after the Y-junction, $W_Y = 50$ μm, the width after the second cross junction, $W_c = 75$ μm, the channel height, $h = 30$ μm and the distance between two consecutive loops, $D_l = 140$ μm. For co-encapsulation and alginate hydrogel devices, an additional aqueous phase inlet was added to the initial design for the sheath flow.

The microfluidic devices were fabricated by a standard soft lithography technique.[27–29] Briefly, SU-8 photoresist was spin-coated onto a 6-inch silicon wafer (Silicon Quest International, Santa Clara, CA) and patterned through UV light exposure at 365 nm using a photomask. The photomask was generated using computer-aided design (CAD) software (AutoCAD 2022, Autodesk, Inc., Dan Rafael, CA) and printed onto a high-resolution transparency sheet (Fineline Imaging, Colorado Springs, CO). After UV exposure, the SU-8 photoresist was developed in propylene glycol monomethyl ether acetate (PGMEA; Sigma-Aldrich, Oakville, ON). Following rinsing and drying steps, the silicon wafer was ready for polydimethylsiloxane (PDMS) replica molding process.

The PDMS slab was prepared using a 10 : 1 ratio mixture of PDMS resin to curing agent (Sylgard 184, Dow Corning, Midland, MI). After degassing, the mixture was poured onto the prepared silicon master followed by curing in an oven at 80 °C for 2 h. Upon PDMS slab removal, inlet and outlet access holes were made using 0.75 mm diameter biopsy punches (Integra Miltex, Inc., Rietheim-Weilheim, Germany). After cleaning, the PDMS slab was irreversibly bonded to a glass slide using oxygen plasma treatment (500 mTorr, 30 W, 30 s, Harrick Plasma, Ithaca, NY). Prior to use, the microfluidic channels were rendered hydrophobic by coating with Aquapel.[30] Fluidic tubing (0.25 mm, O.D. 1.0 mm; IDEX Health & Science, Oak Harbor, WA) was inserted into the inlets and outlets of assembled devices for chip-to-world interfacing.

Experimental setup and droplet generation

Droplets were generated by introducing water and oil phase into their respective channels using a programmable syringe pump (neMESYS; Cetoni, GmbH, Korbussen, Germany) and precision glass syringes (250 μL and 1000 μL; Zinsser NA,

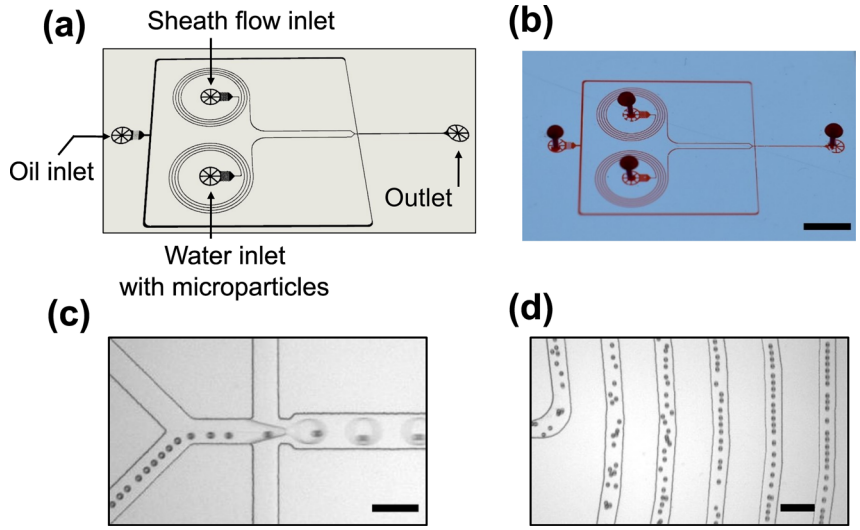

Fig. 1 (a) Schematic design for the sheath flow-controlled microparticle encapsulation in the spiral channel. (b) An image of the fabricated microfluidic devices. To aid visualization, a red dye is used to fill the microfluidic channels. The scale bar is 5 mm. (c) An experimental image of sheath flow-regulated microparticle spacing after the Y-junction. The evenly spaced microparticles are subsequently encapsulated by the oil phase at the T-junction. (d) A representative image showing self-ordering in the spiral channel. The scale bars in (c) and (d) are 100 μm

Northridge, CA). For self-ordering experiments, the microparticles were suspended in a premixed solution of OptiPrep™ density gradient medium (Sigma-Aldrich, St Louis, MI) and phosphate-buffered saline with 0.1% Tween 20 (PBST) at a mixing ratio of 1 : 5.8 (volume ratio). The continuous phase consisted of fluorinated carrier oil (Novec 7500 Engineered Fluid; 3M, St Paul, MN) containing 2% (w/v) 008-FluoroSurfactant (RAN Biotechnologies, Beverly, MA). Typically, the aqueous phase flow rate containing suspended microparticles was set to 10 μL min^{-1}, the oil phase flow rate was set to 50 μL min^{-1}, while the sheath flow rates were varied in the range from 0 to 20 μL min^{-1}. The sheath flow and the microparticle suspended flow are merging together, $Q_s + Q_m = Q_w$, where Q_s represents sheath flow rate, Q_m represents microparticle suspended flow rate and Q_w represents total water flow rate after merging.

Experimental videos and images were recorded using an upright Eclipse LV150N microscope Eclipse LV150N microscope (Nikon, Melville, NY) with 10× or 20× objectives equipped by a high-speed camera (FASTCAM Mini AX200, Photron, San Diego, CA). The acquired images were post-processed using ImageJ software to measure the size of the droplets. The videos were analyzed with a video processing program, VirtualDub, to assess encapsulation efficiency.

Theoretical modeling

The numerical simulation was performed using Incompressible Navier–Stokes module of the COMSOL Multiphysics 3.4. The computational domain comprised approximately 300 K tetrahedral finite elements corresponding to around 1.28 M degrees of freedom. The domain was filled with water-like fluid of mass density ρ = 1000 kg m^{-3} and viscosity η = 1 mPas. Wall type boundary conditions were imposed at around the computational domain, except for the two inlets and the outlet. Constant laminar inflow was specified for the inlets while zero pressure with no viscous stress was imposed at the outlet. We used the default linear system (stationary) solver for the problem and imposed 10^{-6} and 25 as the relative tolerance and the maximum number of iterations, respectively. The solution (fluid velocity field) was plotted in a contour fill plot format and the streamline through the center of the particle inlet channel was constructed. Subsequently, particles spacings on the two sections of the streamline (in the inlet channel and after the junction) were computed using the equation of continuity. The deflection of particles induced by the sheath flow from the other channel was considered, taking into account the distance between the streamline and the wall in the merging channel.

We have also elaborated a 2D analytical model for predicting the distance with respect to the wall and the interparticle spacing after hydrodynamic focusing in the merging channel. By assuming Newtonian and low Reynolds number (Re) flows in both microparticle and sheath channels, we demonstrate that the distance at which microparticles are hydrodynamically focused with respect to the wall can be approximated as:

$$d_w(x) = \frac{aQ_m}{2(Q_m + Q_s)} \quad (1)$$

where a is the width of the merging channel, Q_m and Q_s are the flow rates in the microparticle and sheath channels and $x = aQ_m/(Q_m + Q_s)$.

As for the interparticle distance, we demonstrate in a similar manner that the distance ε between microparticles in the hydrodynamically focused flow can be approximated as:

$$\varepsilon(x) = \zeta \frac{\varepsilon_m a h}{Q_m} u_{avg}(x) \quad (2)$$

ε_m is the interparticle spacing in the entering microparticle channel, h is the height of the merging channel and u_{avg} is the average flow velocity in the hydrodynamically focused microparticle flow. Here ζ is an empirical fitting factor accounting for the limitations induced by the two-dimensional approximation for the flow. The full derivation of both eqn (1) and (2) are given in SI, section 1. Analytical modeling of particle interspacing in hydrodynamically focused flows.

Cell culture

Human T lymphoblasts (Jurkat, TIB-152™, ATCC, Manassas, VA) and monocyte (THP-1, TIB-202™, ATCC) were cultured in a T-25 flask in RPMI-1640 medium (Gibco) supplemented with 2 mM glutamine, 10% fetal bovine serum (FBS, Gibco, Montana, MT), 1% penicillin (100 units per mL), and streptomycin (100 μg mL^{-1}) at 37 °C and incubator with 5% CO_2. The passage numbers of the Jurkat cells and THP-1 monocytes were P3-P6 and P3-P4, respectively.

The THP-1 monocytes were differentiated into macrophages overnight by supplementing 0.2 μg mL^{-1} phorbol 12-myristate 13-acetate (PMA) (Sigma-Aldrich) followed by 24 h culture in RPMI-1640 medium.[31,32] This differentiation of macrophages was confirmed using a 24-well plate format by observing morphological changes. For macrophage cytokine release experiments in droplets, we suspended the cells with 0.2 μg mL^{-1} PMA and 0.4 μg ml^{-1} of lipopolysaccharides from *Escherichia coli* O26:B6 (LPS) (Sigma-Aldrich) in RPMI-1640 medium.

For cell ordering experiments, the Jurkat cells were suspended in 16% OptiPrep and 0.01% Triton-X in a PBS buffer (RPMI for THP-1 cell experiments) at an approximate concentration of 20×10^6 cells per mL.[13] Cells were introduced in the channel at a flow rate of 10 μL min^{-1}. For ordering experiments, a buffer solution (0.01% Triton-X in a PBS buffer) was used to pinch the flow. Fluorinated oil (2%) was used to generate droplets. The resulting emulsion was collected at the outlet of the droplet generator and transferred into a tube.

Magnetic microbead immunoassay

Cytokine immunoassay was performed using magnetic microbeads. Approximately, 70×10^6 streptavidin-coated superparamagnetic microbeads (2.8 μm, M-270 Streptavidin, Invitrogen, Waltham, MA) were transferred to a 1.5 mL microcentrifuge tube and placed in a magnetic stand to remove storage buffer, follow by a wash with 250 μL D-PBS (Gibco). The microbeads were then incubated with 5 μg of anti-human TNF-α biotinylated antibody (R&D Systems, Minneapolis, MN) in 200 μL D-PBS for 90 min on an orbital shaker. Following functionalization, microbeads were washed four times with 0.1% v/v Tween-20 (Sigma-Aldrich) in D-PBS (PBST). Microbeads were then blocked with 1% w/v bovine serum albumin (Sigma-Aldrich) in PBST for 1 hour on an orbital shaker and washed four times with PBST and stored at 4 °C.

For microfluidic droplet experiments, magnetic microbeads were co-encapsulated with THP-1 cells containing PMA and LPS stimulants. Prior to the cell stimulation experiments, we assessed the co-encapsulation efficiency of THP-1 cells and magnetic beads by suspending them on each side of the spiral channels. The concentrations of THP-1 and magnetic microbeads were approximately 17–20 × 10^6 mL^{-1} and 35 × 10^6 mL^{-1}, respectively. In the cytokine detection experiment, the water-in-oil droplets were incubated for 24 hours to allow for cell stimulation, activation and subsequent binding of the released cytokines to the microbeads. Non-stimulated droplets were also examined as a control. Following microbead collection step using a magnetic separation rack, the pooled microbeads were incubated with 5 μg mL^{-1} human anti-TNFα antibody (R&D Systems) for 2 hours in D-PBS on an orbital shaker. Subsequently, the microbeads were washed 4 times with PBST and then exposed to 200 μL of 5 μg mL^{-1} Alexa Fluor® 488 Goat anti-mouse IgG (Biolegend, San Diego, CA) for 30 min. Following another wash step, microbeads were imaged using the EVOS XL Core microscope system (Thermo Fisher Scientific, Waltham, MA).

Alginate microgel generation

Alginate microgels were generated by adapting previously published work.[33] Briefly, two aqueous solutions of a zinc-rich solution (Zn-EDDA) and a calcium-rich solution (Ca-EDTA) were prepared separately. The Zn-EDDA solution was prepared by mixing 84 mM zinc acetate (Zn) (Sigma-Aldrich), 84 mM ethylenediamine-*N*,*N*′-diacetic acid (EDDA) (Sigma-Aldrich), 40 mM HEPES and 1 wt% alginate (Novamatrix, Sandvika, Norway) in *N*-(2-hydroxyethyl)piperazine-*N*-2-ethane sulfonic acid (HEPES) buffered saline (HBS) (Sigma-Aldrich). The Ca-EDTA solution was prepared by mixing 84 mM calcium chloride (Ca) (Sigma-Aldrich), 84 mM ethylenediaminetetraacetic acid (EDTA) (Sigma-Aldrich), 40 mM HEPES pH 7.4 and 1 wt% alginate in HBS. Cells were suspended in 16% OptiPrep™ density gradient medium and 0.01% Triton-X in RPMI-1640 medium.[34] The prepared solutions were filled in precision glass syringes and alginate droplet generation experiments were performed by placing the microfluidic device on the microscope stage for observation. Following gelation, the alginate microgels were released from the emulsion in two steps. The excess oil was first removed from the bottom layer of the phase, followed by addition of 20% vol of 1*H*,1*H*,2*H*,2*H*-Perfluoro-octanol (PFO) (Sigma-Aldrich) in Novec 7500 to destabilize the emulsion. The solution was mixed by pipetting up and down to fully saturate the droplet surface, while minimizing perturbation of the top medium layer.[35] The released gels located in the top medium phase were then collected by pipetting.

Results and discussion

Single microparticle encapsulation

For single microparticle encapsulation, we implemented high concentrations of microparticles in a microfluidic device inte-

grating spiral microchannels for on-chip sample dilution, microparticle ordering and droplet formation. Fig. 1 shows the schematic microfluidic device design and an example of a fabricated device. A pair of spiral channels is used to suspend the microparticles and modulate the water inlet ratio through sheath flow. Geometry of the spiral channels (width, height, curvature radius and number of turns) was designed according to the theoretical model developed by Clime *et al.*[36] Two junctions are clearly shown in Fig. 1c. At the first Y-junction, a pinched flow channel is adjusting the space between microparticles by utilizing the sheath flow arriving at the junction through the top channel. Subsequently, the microparticles are encapsulated by the oil phase, forming droplets at the second cross junction.

For these experiments, microparticles with a diameter of 15 μm were prepared at a concentration of 20×10^6 particles per mL and delivered into the microfluidic chip *via* a spiral channel inlet. Due to inertial focusing effects, the suspended microparticles self-order downstream of the spiral channel. Notably, after the fourth spiral loop, we observed that the microparticles formed well-defined trains (Fig. 1d). The interparticle distance is further regulated by the sheath flow, leading to the encapsulation of evenly spaced microparticles by the oil phase at the second junction (Fig. 1c).

Flow dynamics and droplet formation regimes

Prior to characterization of microparticle encapsulation efficiency, we systematically investigated flow dynamics at the second junction to confirm droplet generating regimes by adjusting inlet flow rates Q_o and Q_w, where Q_o is the flow rate of the oil phase and Q_w is the total flow rate of the aqueous phase. Fig. 2 depicts the experimental results as a phase diagram, identifying physically meaningful droplet generation regimes over a range of flow rate ratios Reynolds number (Re) values, along with images of the topology of the generated droplets for each regime. We observed that discrete droplets were formed at the flow rate ratio Q_o/Q_w in the range of $2.1 \leq Q_o/Q_w \leq 14$ as indicated by the solid circles in the graph. We also identified other flow regimes such as wave jetting (solid triangles, at $1.2 \leq Q_o/Q_w \geq 2$) and long jetting (empty diamonds, at $Q_o/Q_w \leq 1.2$). These results show a classification scheme that is similar to the ones published previously.[37] To enable inertial focusing effects of the beads in the spiral channels,[10,36] the aqueous phase flow rate was set to 10 μL min^{-1} (Re = 4.2), within the inertial regime, while the oil phase flow rate was fixed at 50 μL min^{-1}. The aqueous sheath flow rate was varied from 0 to 20 μL min^{-1} to modulate the spacing between the concentrated microparticles.[4] Here, the capillary number $Ca = \mu_c u_c/\sigma = 0.02$, where μ_c, u_c, σ represent the dynamic viscosity, the velocity of the continuous phase and the interfacial tension between the dispersed and the continuous phase, respectively. The range of values for the Ca number that mapped the dripping regimes is similar to the finding in the literature.[38,39]

It is noteworthy that by introducing flow rates of 20 μL min^{-1} for the total aqueous phase and 50 μL min^{-1} for the oil phase, the generated droplets were highly monodispersed with a size of approximately 56 μm ± 1.3, and a coefficient of variation (CV) of 2.3%. The droplet production rate has reached over 3050 droplets per second (see SI Fig. S1).

Effects of the hydrodynamic pinched flow and single particle encapsulation efficiency

Fig. 3 presents experimental results depicting the distribution of microparticles utilizing sheath flow, accompanied by a comparative study with our computational model using COMSOL Multiphysics. Initially, suspended microparticles underwent a self-organization process in the upstream spiral region, forming a structured arrangement downstream owing to inertial effects. As they approached the Y-junction channel, the microparticles became subject to the influence of sheath flows. Fig. 3(a–d) display representative images illustrating the impact of varying sheath flow rates (*e.g.* 0, 5, 10 and 20 μL

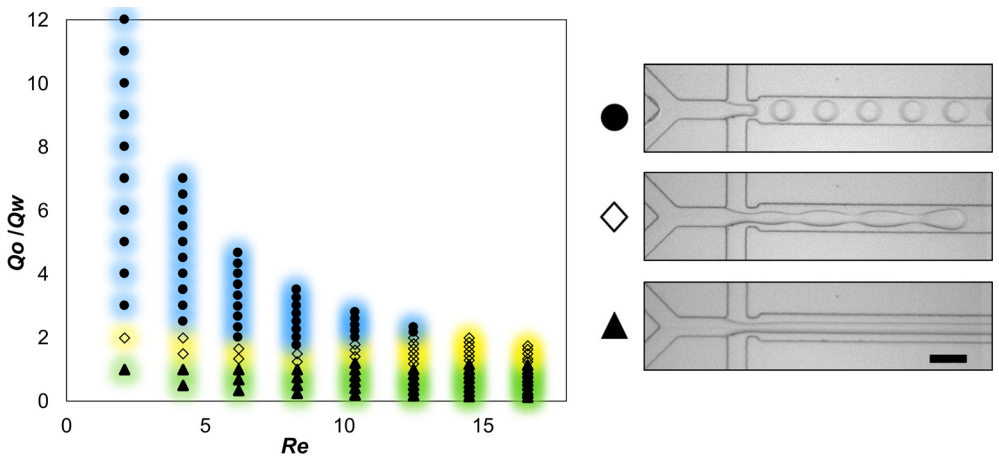

Fig. 2 Phase diagram of droplet generation regimes with varying flow rates of oil and water (left). Q_o and Q_w represent oil flow rate and total flow rate after the first junction. Representative images of droplet formation and flow patterns (right): droplet formation (solid circles), waved jetting (empty diamonds), and jetting (solid triangles). The scale bar is 100 μm.

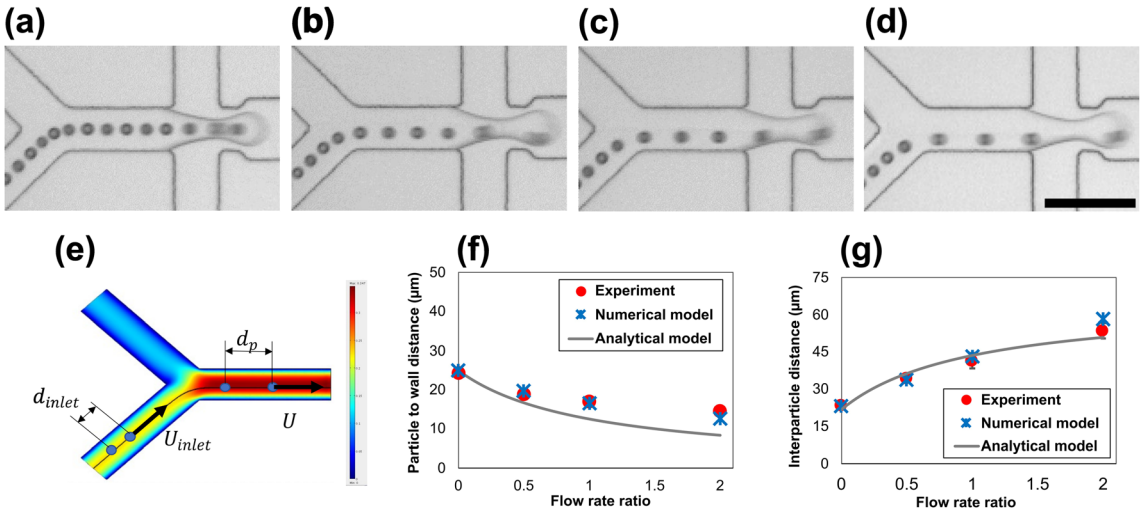

Fig. 3 Images of microparticles distribution using the sheath flow. (a)–(d) represent the sheath flow rates of 0, 5, 10 and 20 μL min^{-1}, respectively. The scale bar is 100 μm. (e) Microparticle trajectory simulation at the first junction using COMSOL Multiphysics. The simulation was performed 3D incompressible Navier–Stokes using 500k elements. The colors represent the contour fill plot of the velocity. (f) and (g) Histograms showing particle-to-wall distance and interparticle distance as a function of the flow rate ratio in comparison with numerical and analytical models.

min^{-1}), corresponding to flow rate ratios (Q_s/Q_m) of 0, 0.5, 1 and 2, respectively. Our observations revealed that an increased sheath flow led to a shift in microparticles towards the channel side wall, effectively lengthening the spacing between microparticles due to the hydrodynamic forces. We quantified both particle-to-particle distance and particle-to-wall distance in response to varying sheath flow rates. As anticipated, the increase in flow rate ratio corresponded to an augmented interparticle separation and a diminished particle-to-wall distance. Specifically, the interparticle distance exhibited a range from 23 μm to 54 μm, while the particle-to-wall distance varied between 24 μm and 15 μm. We also investigated interparticle separation under varying inlet flow conditions to evaluate the stability of the particle expansion ratio with respect to the flow rate ratio. The expansion ratio, defined as D_f/D_i, where D_i is the interparticle distance before the Y-junction and D_f is the distance after, was quantified through image analysis. The results showed no significant variation in the expansion ratio across flow rates of 7, 10 and 15 μL min^{-1}, when the flow rate ratio was held constant (see SI Fig. S2).

To complement the analysis, we compared the experimental data with both the analytical model and numerical 3D finite element simulations to predict microparticle trajectories (Fig. 3e–g). While the analytical model shows some deviation in particle-wall distance at higher flow rate ratios (Fig. 3f), both models exhibit relatively good agreement at lower flow rate ratios. The slight discrepancy observed at higher flow rate ratios can be attributed to the limitations of the simplified 2D analytical model, as the 2D approximation of the liquid flow cannot account for wall effects arising from inertial focusing mechanisms and the no-slip boundary conditions at the top and bottom channel walls.

The self-organized microparticles were subsequently encapsulated by the oil phase after passing through the flow focusing junction, as demonstrated in SI Movies 1 and 2, with sheath flow rate ratios of Q_s/Q_m = 0 and 1, respectively. We compare the single microparticle encapsulation rate *vs.* Poisson statistics at different ratios of sheath flow (Fig. 4a–d). The Poisson statistics P is represented by the following equation;

$$P_k = \frac{\lambda^k}{k!}\exp(-\lambda) \quad (3)$$

where, k is the number of 0, 1, 2 and 3 microparticles in the droplet and λ is the average number of microparticles per droplet.

In the absence of the sheath flow, the single-particle encapsulation efficiency was found to be approximately 34%, closely aligned with the calculated Poisson distribution of 32%. For two particle configurations, encapsulation efficiency was higher at 63%, contrasting with the Poisson distribution value of 26%, given the droplet volume of approximately 95 nL (refer to Fig. 4a). However, with the introduction of the sheath flow (Fig. 4b), the efficiency of both single and two-particle encapsulation efficiencies underwent significant alterations (Fig. 4b). Notably, at high sheath flow ratios of 1 and 2, we achieved a single-particle encapsulation rate exceeding 76%, two-fold increase compared to the Poisson distribution (Fig. 4c and d). Although a recent numerical and analytical study of flow-focusing droplet generation predicts that 100% encapsulation efficiency is theoretically achievable under the dripping regime,[40] achieving this experimentally remains challenging. These limitations primary arise from transport instabilities at high particle volume fractions and non-ideal longitudinal ordering, unless downstream strategies, such as droplet sorting[41] or pre-coating and sampling process,[42] are

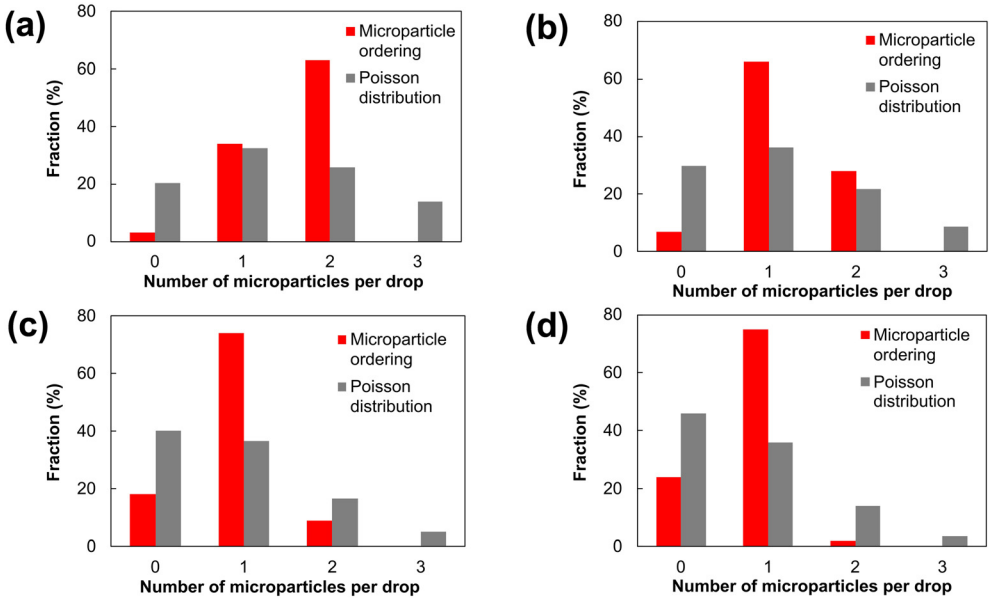

Fig. 4 Comparative study of sheath flow-induced single microparticle encapsulation rate. Histograms show Poisson statistics and normalized frequency of droplets containing the specified number of particles. The sheath flow rate ratios are given as 0, 0.5, 1, and 2, for panels (a), (b), (c), and (d), respectively, (n = 416, 424, 457 and 438 droplets and λ = 1.60, 1.21, 0.91 and 0.78, respectively).

implemented. Nevertheless, our encapsulation efficiency achieves yields comparable to prior reports while enabling controllable suspension density and downstream encapsulation through on-chip pinch flow control.[10]

To evaluate on-chip control of the λ values, we further performed a comparative study of encapsulation efficiency under two different initial conditions. Microparticles at distinct starting concentrations were suspended and introduced into the microfluidic device. By modulating the flow rate ratio, identical λ values could be achieved despite differences in the initial particle concentrations (see SI Fig. S3). This capability further distinguishes our approach from conventional inertial focusing-based self-ordering methods, which lack such independent control over encapsulation statistics.

Single-cell encapsulation and co-encapsulation with magnetic microbeads

The activation of blood cancer cells, such as leukemia cells, and the detection of their secreted cytokines using barcoded beads is the main motivation behind our current study.[43] The technological challenge lies in detecting cytokines at the single-cell level in a high throughput manner. A significant stride in this direction is the achievement of highly efficient microfluidic encapsulation of self-ordered cells. To demonstrate the effectiveness sheath flow assisted self-ordering for cell encapsulation in our approach, we conducted experiments with Jurkat cells using the same two-inlet spiral channel design (Fig. 5a). In these experiments, the cell suspension solution was introduced at a flow rate of 10 μL min^{-1}, while the sheath flow and continuous phase were maintained at 10 μL min^{-1} and 50 μL min^{-1}, respectively. Notably, we observed that dispersed cells became ordered after the fourth loop and were subsequently encapsulated by the oil phase at the cross junction (Fig. 5a). Cells that underwent ordering in the sheath flow-controlled channel were directed to the side wall before reaching the cross junction (Fig. 5c), whereas cells without sheath flow control remained dispersed in their flow (Fig. 5b).

Additionally, we conducted a comparative analysis by plotting histograms of Poisson statistics and the normalized frequency of droplets containing a specific number of cells. These plots correspond to different sheath flow rate ratios of Q_s/Q_m = 0, 1 and 2 in Fig. 5d, e and f, respectively. Our analysis revealed that the droplet's single-cell capture efficiency using sheath flow exceeded 60%, representing again a significant improvement compared to the Poisson distribution. Conversely, most encapsulations ranged from 0 to 3 cells.

To showcase the co-encapsulation capabilities, we conducted experiments involving microparticles introduced into two distinct spiral channels. The resulting images reveled the formation of microparticle trains and co-encapsulation at the cross junction with both spiral channels exhibiting microparticle self-ordering behavior after the fourth loop. Subsequently, the self-ordered particles were seamlessly co-encapsulated by the oil phase, aligning with our expectations (see SI Fig. S4a–c). The co-encapsulation capture efficiency was calculated using the following equation;

$$P(k_T \cap k_B) = \frac{\lambda^{k_T}}{k_T!}\exp(-\lambda_T) \times \frac{\lambda^{k_B}}{k_B!}\exp(-\lambda_B) \quad (4)$$

where k_T and k_B represent the number of microparticles located on the upper and lower parts of the droplet, respectively (see SI Fig. S4c).

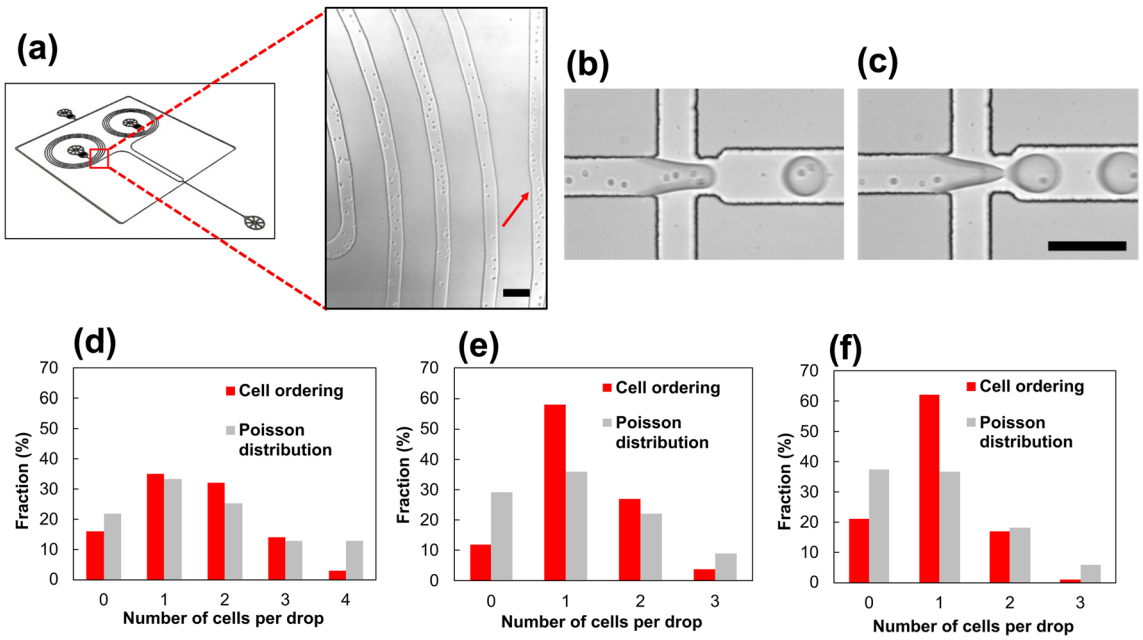

Fig. 5 Microfluidic device used for cell encapsulation experiments. (a) An image of the device design used for cell experiments. A zoomed-in inset shows cell ordering within the spiral channel. The arrow indicates the loop channel employed for cell ordering. (b and c) Micrographs showing cell distribution and encapsulation with the sheath flow rate ratios of 0 and 1, respectively. (d–f) Histograms showing cell encapsulation rate compared to the Poisson distribution (n = 276, 165 and 146 drops and λ = 1.53, 1.23 and 0.98, respectively). The sheath flow rate ratios are given as 0, 1, and 2 for panels (d), (e) and (f), respectively. The scale bars are 100 μm.

The resulting analysis showed that we successfully attained a one-to-one co-encapsulation efficiency exceeding 53%, representing a fourfold improvement over the co-encapsulation rate limited by the Poisson distribution (see SI Fig. S4d).

To further demonstrate the application of single cell and multiple magnetic beads co-encapsulation capabilities, we also performed experiments to assess the co-encapsulation efficiency of THP-1 cells with magnetic beads. In this context, our goal was to encapsulate one cell and more than one magnetic bead per droplet for cytokine detection. Experimentally, the THP-1 cell suspension was introduced through one aqueous inlets at a flow rate of 10 μL min^{-1}, while the magnetic bead suspension was delivered through the second aqueous inlet (Fig. 6a). The bead flow rate was set to 5, 10 and 15 μL min^{-1}, corresponding to the flow rate ratios of Q_b/Q_c = 0.5, 1, and 1.5, where Q_b and Q_c denote the magnetic bead and cell suspension flow rates, respectively. The continuous phase flow rate was maintained at 50 μL min^{-1}, consistent with previous experiments.

Fig. 6b–d shows the comparative study of co-encapsulation efficiencies of cells and magnetic beads. We observed that as the Q_b/Q_c ratio increases from 0.5 to 1 and 1.5, a greater number of magnetic beads are co-encapsulated, whereas the number of co-encapsulated cells decreases, as anticipated. However, the one-cell-to-one-magnetic-bead co-encapsulation efficiency does not reach the same level as that observed for the co-encapsulation of 15 μm diameter microparticles. We believe this lower efficiency is due to differences in the physical properties of the encapsulated objects. The co-encapsulation efficiency of the cells and magnetic beads is a result of combined effects of the self-ordering of cells and the random distribution of magnetic beads within the channels. Specifically, cells are influenced by initial focusing effects in the spiral channel and sheath flow, while the small magnetic beads are not.[9] We believe the size of magnetic beads impacts self-ordering and subsequent encapsulation efficiency. As the Reynolds number and the inertial lifting force are proportional to the size of particle, smaller particles experience weaker inertial forces and consequently exhibit reduced ordering quality.[44] Nevertheless, in our single cell analysis approach, it is preferable to include multiple magnetic beads per cell within droplets. The experimental results showed that the one-cell-multiple-beads co-encapsulation efficiency reaches 40%, a significant improvement compared to the sum of Poisson distribution (Table 1). This one-cell-multiple-beads co-encapsulation strategy is advantageous for multiplexing immunoassay at the single cell level as demonstrated in our recent work using a particles-in-particle system.[45]

Cytokine immunoassays using magnetic beads

Single-cell-level cytokine detection provides valuable insights into individual cells and their cytokine production, facilitating crucial applications such as cytokine profiling of the immune cells[46] and investigating cancer cell-to-immune cell interactions for immunotherapy.[47] To demonstrate the effectiveness of our approach for single-cell-level cytokine detection, we performed a magnetic bead-based cytokine immunoassay using differentiated THP-1 macrophages.[48] THP-1, a human leuke-

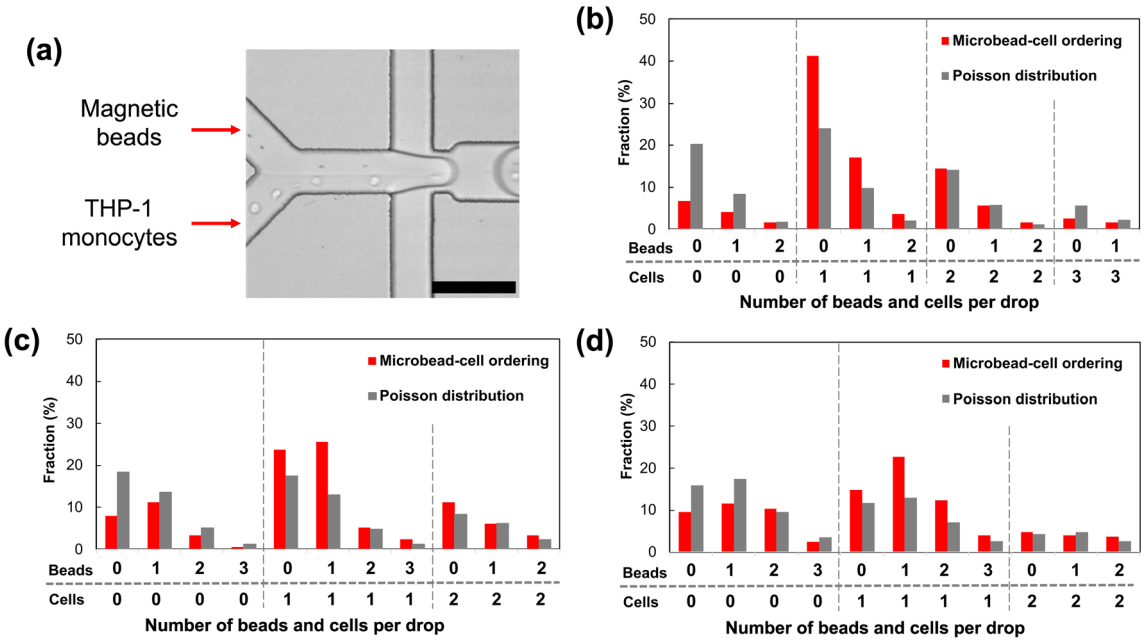

Fig. 6 Comparative study of co-encapsulation efficiency of cells and magnetic beads. (a) A representative image of the co-encapsulation of THP-1 monocytes and magnetic beads in droplets. The scale bar is 100 μm. Histograms show double Poisson distribution and co-encapsulation of THP-1 cells and magnetic beads with; (b) the flow rate ratio Q_b/Q_c of 0.5 (n = 194 droplets, λ = 0.41 and 1.18 with beads and cells, respectively), (c) the flow rate ratio Q_b/Q_c of 1 (n = 215 droplets, λ = 0.74 and 0.95 with beads and cells, respectively) and (d) the flow rate ratio Q_b/Q_c of 1.5 (n = 251 droplets, λ = 1.10 and 0.75 with beads and cells, respectively).

Table 1 A comparative study of cell and magnetic bead co-encapsulation efficiency as a function of flow rate ratio

Flow rate ratio (Q_b/Q_c)	0.5	1	1.5
Cells (λ)	1.18	0.95	0.75
Magnetic beads (λ)	0.41	0.74	1.10
One cell + multiple beads[a]	21%	33%	39%
Sum of Poisson distribution	12%	19%	23%

[a] The percentages indicate experimental and Poisson encapsulation efficiencies.

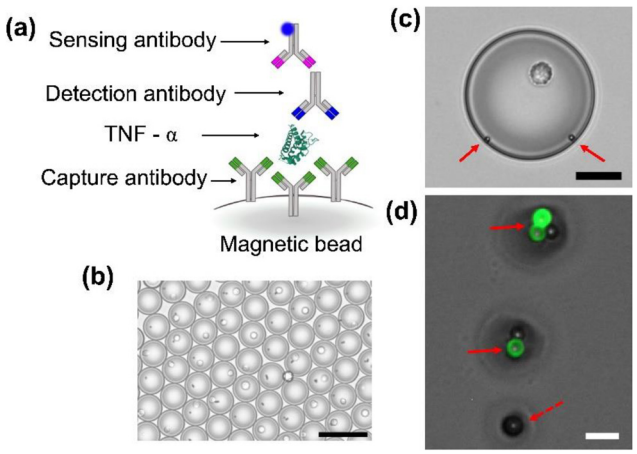

Fig. 7 Single-cell cytokine detection using magnetic beads. (a) A schematic of magnetic bead-based immunoassay. (b) A representative image of encapsulated cells and magnetic beads in water-in-oil droplets. The scale bar is 100 μm. (c) A zoomed in image showing co-encapsulation of a single cell with beads. Red arrows indicate magnetic beads. The scale bar is 20 μm. (d) A merged fluorescent and bright-field image. The secreted cytokine is detected by the magnetic beads shown in the green fluorescence, indicated by the red arrow bars. Here, the magnetic beads were pooled together from the sample. A dashed arrow indicates a control bead. The scale bar is 5 μm.

mia monocytic cell line, serves as an excellent model for immune modulation studies. THP-1 monocytes are differentiated into M0 macrophages through PMA treatment. These M0 macrophages are then polarized into M1 macrophages through LPS stimulation, characterized by proinflammatory cytokines such as TNF-α, IL-1β, IL-6, IL-12, IL-18 and IL-23.[49]

In our cytokine immunoassay experiments, THP-1 cells were suspended in a PMA/LPS solution before microfluidic device encapsulation, with morphological changes of the THP-1 cells illustrated in SI Fig. S5. The specific target for our study was the secreted cytokine TNF-α, for which we employed biotin-conjugated anti-TNF-α antibodies immobilized on streptavidin-coated magnetic beads (Fig. 7a). By introducing the magnetic beads in the sheath channel inlet, we co-encapsulated them with THP-1 cells in droplets (Fig. 7b). Fig. 7c shows a representative image of the co-encapsulated THP-1 and two magnetic beads. We then cultured cells for 24 hours to capture secreted cytokine onto functionalized magnetic beads. The cytokine-bound magnetic beads were isolated from droplets using the magnetic separation rack. Following the detection antibody and sensing antibody binding steps, we successfully

identified the presence of TNF-α through fluorescence imaging (Fig. 7d), confirming the applicability of our microfluidic approach for single-cell cytokine detection.

Additionally, in order to demonstrate the cytokine detection capability within commonly employed hydrogel formats, we also conducted cell encapsulation in an alginate hydrogel as shown in SI Fig. S6. For this application, we designed three aqueous spiral channels featuring one cell suspension inlet and two pre-polymer solutions inlets (see SI Fig. S6a). The two pre-polymer solutions comprised an alginate precursor containing Zn-EDDA and alginate containing Ca-EDTA. The ion exchange between the Zn^{2+} and Ca^{2+}during droplet formation and mixing facilitated crosslinking of the alginate, resulting in the overall encapsulation of cells within the hydrogel.[33] Within the alginate hydrogel format, we conducted a cytokine immunoassay by co-encapsulating THP-1 cells and anti-TNF-α conjugated magnetic beads. This investigation also confirmed successful detection of the released cytokine, TNF-α, on the magnetic beads (see SI Fig. S6f). Detailed quantitative analysis of alginate droplet-based TNF-α detection using fluorescence intensity barcoded magnetic microparticles has been reported in our recent work.[45] The present study therefore serves as a proof-of-concept demonstration that the enhanced encapsulation efficiency enabled by the sheath-flow assisted spiral-channel system could be directly applied to quantitative, multiplexed cytokine detection at the single-cell level.

Conclusions

The encapsulation of microparticles in microfluidic channels represents a powerful method with broad applications in single-cell analysis. In this manuscript, we demonstrated a sheath flow-assisted passive microparticle (co)-encapsulation technique with a spiral channel. Operating within the inertial focusing regime, suspended microparticles undergo self-ordering downstream of the spiral loops. The addition of a hydrodynamic sheath flow focusing junction proves instrumental in adjusting the interparticle distance and repositioning them for subsequent encapsulation within a continuous oil phase. Notably, our observations reveal that as the sheath flow ratio (Q_s/Q_m) increases from 0 to 0.5, 1 and 2, the microparticles shift towards the side channel wall, and interparticle distance lengthens due to the hydrodynamic focusing effects. The experimentally measured particle positions show good agreement with theoretical predictions from both numerical and analytical models. Moreover, the observed hydrodynamic migration and the resulting expansion in interparticle spacing are independent of the inlet flow rates of the suspended microparticles. Through hydrodynamic focusing, this on-chip modulation of interparticle distance leads to a high-yield single-particle encapsulation efficiency, exhibiting a two-fold increase over Poisson statistics with sheath flow ratios of 1 and 2. Additionally, our on-chip dilution approach allows for *in situ* modulation of the λ value achieving an optimal number of encapsulating microparticles. While the pinched flow concept has been previously demonstrated for continuous particles fractionation,[50,51] droplet sorting,[24] and cell encapsulation,[21] our work stands out by utilizing highly concentrated, self-ordered microparticles.

Although inertial flow focusing is a widely used pre-ordering method for particles and cells, it offers limited control over sample concentration and requires fixed flow rates, which can be restrictive in variable experimental conditions.[18] In contrast, our approach provides a versatile alternative, enabling precise tuning of microparticle spacing and modulation of capture efficiency, thereby offering enhanced operational flexibility and broader practical applicability. By adjusting hydrodynamic sheath flow rates, we can effectively reposition microparticles and subsequently encapsulate them in the oil phase. We believe that the proposed concept holds significant promise for applications requiring tunable cell encapsulation, ranging from multicell to single-cell formats, such as circulating tumor cell analysis[52] and body fluid processing, including sperm isolation.[53]

To showcase the co-encapsulation capability, we presented one-to-one single particles and cells-to-magnetic beads co-encapsulation. In future investigations, we plan to delve into particle pairing studies at varying ratios, particularly for applications involving multicellular aggregations[52] Additionally, we aim to explore tumor-CAR-T cell co-encapsulation, focusing on understanding cell-to-cell interactions, and cytokine release functionality and potency.[54,55]

Finally, we successfully demonstrated single cell encapsulation and protein cytokine detection utilizing magnetic beads. By co-encapsulating together with THP-1 cells and anti-TNF-α conjugated magnetic beads, we could identify the presence of the secreted cytokine, TNF-α, induced by PMA/LPS treatment in both aqueous droplets and alginate hydrogels. Building upon the successful detection of single-cell protein secretion using a multiplexed sandwich immunoassay implemented on barcoded magnetic microbeads,[45] this approach aims to quantify the concentration of cytokines from single cells.[56] We anticipate that our proposed method will extend its applicability to areas such as single cell sequencing[8] and activation of CAR-T cells through the co-encapsulation with leukemia cells, enabling comprehensive cytokine profiling.

Author contributions

Byeong-Ui Moon: conceptualization, methodology, data curation, investigation, writing – original draft, Lidija Malic: conceptualization, review & editing, project administration, funding acquisition, Dillon Da Fonte: methodology, writing, Liviu Clime: methodology, theoretical modeling, review & editing, Félix Lussier: methodology, review & editing, Ljuboje Lukic: methodology, David Juncker: conceptualization, review & editing, project administration, funding acquisition, Teodor Veres: conceptualization, project administration, funding acquisition.

Conflicts of interest

The authors declare that they have no known competing financial interests or personal relationships that could have appeared to influence the work reported in this paper.

Data availability

The data supporting this article have been included in the main text and the supplementary information (SI). Supplementary information: analytical modeling, Fig. S1–S6 and movies. See DOI: https://doi.org/10.1039/d5an00986c.

Acknowledgements

This work was supported by the National Research Council Canada from the Cell and Gene Therapy Challenge program.

References

1 T. Stuart and R. Satija, *Nat. Rev. Genet.*, 2019, **20**, 257–272.
2 V. Chokkalingam, J. Tel, F. Wimmers, X. Liu, S. Semenov, J. Thiele, C. G. Figdor and W. T. S. Huck, *Lab Chip*, 2013, **13**, 4740–4744.
3 W. Zhou, Y. Yan, Q. Guo, H. Ji, H. Wang, T. Xu, B. Makabel, C. Pilarsky, G. He, X. Yu and J. Zhang, *J. Nanobiotechnol.*, 2021, **19**, 1–21.
4 D. J. Collins, A. Neild, A. deMello, A. Q. Liu and Y. Ai, *Lab Chip*, 2015, **15**, 3439–3459.
5 B.-U. Moon, N. Abbasi, S. G. Jones, D. K. Hwang and S. S. H. Tsai, *Anal. Chem.*, 2016, **88**, 3982–3989.
6 D. Liu, M. Sun, J. Zhang, R. Hu, W. Fu, T. Xuanyuan and W. Liu, *Analyst*, 2022, **147**, 2294–2316.
7 D. Holmes, D. Pettigrew, C. H. Reccius, J. D. Gwyer, C. Van Berkel, J. Holloway, D. E. Davies and H. Morgan, *Lab Chip*, 2009, **9**, 2881–2889.
8 R. Zilionis, J. Nainys, A. Veres, V. Savova, D. Zemmour, A. M. Klein and L. Mazutis, *Nat. Protoc.*, 2017, **12**, 44–73.
9 J. M. Martel and M. Toner, *Annu. Rev. Biomed. Eng.*, 2014, **16**, 371–396.
10 E. W. M. Kemna, R. M. Schoeman, F. Wolbers, I. Vermes, D. A. Weitz and A. Van Den Berg, *Lab Chip*, 2012, **12**, 2881–2887.
11 H. S. Moon, K. Je, J. W. Min, D. Park, K. Y. Han, S. H. Shin, W. Y. Park, C. E. Yoo and S. H. Kim, *Lab Chip*, 2018, **18**, 775–784.
12 S. Köster, F. E. Angilè, H. Duan, J. J. Agresti, A. Wintner, C. Schmitz, A. C. Rowat, C. A. Merten, D. Pisignano, A. D. Griffiths and D. A. Weitz, *Lab Chip*, 2008, **8**, 1110–1115.
13 X. Luo and A. P. Lee, *Microfluid. Nanofluid.*, 2023, **27**, 1–12.
14 S. Y. Tang, I. D. Joshipura, Y. Lin, K. Kalantar-Zadeh, A. Mitchell, K. Khoshmanesh and M. D. Dickey, *Adv. Mater.*, 2016, **28**, 604–609.
15 K. Tatsumi, A. Noma, R. Honma, R. Kuriyama and K. Nakabe, *Microfluid. Nanofluid.*, 2021, **25**, 1–13.
16 M. Navi, N. Abbasi, M. Jeyhani, V. Gnyawali and S. S. H. Tsai, *Lab Chip*, 2018, **18**, 3361–3370.
17 D. J. Collins, T. Alan, K. Helmerson and A. Neild, *Lab Chip*, 2013, **13**, 3225–3231.
18 C. He, H. Zhuo, C. Yang, J. Wang, X. Jiang, F. Li, C. Lin, H. Yang, T. Yong, X. Yang, Z. Liu, Y. Ma, L. Nie, G. Liao and T. Shi, *Lab Chip*, 2025, **25**, 2669–2683.
19 L. Nan, Z. Yang, H. Lyu, K. Y. Y. Lau and H. C. Shum, *Adv. Biosyst.*, 2019, **3**, 1–7.
20 L. Nan, M. Y. A. Lai, M. Y. H. Tang, Y. K. Chan, L. L. M. Poon and H. C. Shum, *Small*, 2020, **16**, 1902889.
21 L. Li, P. Wu, Z. Luo, L. Wang, W. Ding, T. Wu, J. Chen, J. He, Y. He, H. Wang, Y. Chen, G. Li, Z. Li and L. He, *ACS Sens.*, 2019, **4**, 1299–1305.
22 H. Onoe, K. Inamori, M. Takinoue and S. Takeuchi, *RSC Adv.*, 2014, **4**, 30480–30484.
23 A. Jeyasountharan, K. Shahrivar, G. D'Avino and F. Del Giudice, *Anal. Chem.*, 2021, **93**, 5503–5512.
24 J. Zhou, A. Wei, A. Bertsch and P. Renaud, *Lab Chip*, 2022, **22**, 4841–4848.
25 T. Tang, H. Zhao, S. Shen, L. Yang and C. T. Lim, *Microsyst. Nanoeng.*, 2024, **10**, 1–12.
26 T. P. Lagus and J. F. Edd, *RSC Adv.*, 2013, **3**, 20512–20522.
27 Y. Xia and G. M. Whitesides, *Annu. Rev. Mater. Sci.*, 1998, 153–184.
28 B.-U. Moon, D. K. Hwang and S. S. H. Tsai, *Lab Chip*, 2016, **16**, 2601–2608.
29 B. U. Moon, L. Clime, J. A. Hernandez-Castro, D. Brassard, C. Nassif, L. Malic and T. Veres, *Langmuir*, 2022, **38**, 79–85.
30 J. F. Edd, D. Di Carlo, K. J. Humphry, S. Köster, D. Irimia, D. A. Weitz and M. Toner, *Lab Chip*, 2008, **8**, 1262–1264.
31 C. Ma, R. Fan, H. Ahmad, Q. Shi, B. Comin-Anduix, T. Chodon, R. C. Koya, C. C. Liu, G. A. Kwong, C. G. Radu, A. Ribas and J. R. Heath, *Nat. Med.*, 2011, **17**, 738–743.
32 M. Genin, F. Clement, A. Fattaccioli, M. Raes and C. Michiels, *BMC Cancer*, 2015, **15**, 1–14.
33 A. G. Håti, D. C. Bassett, J. M. Ribe, P. Sikorski, D. A. Weitz and B. T. Stokke, *Lab Chip*, 2016, **16**, 3718–3727.
34 H. Liu, M. Li, Y. Wang, J. Piper and L. Jiang, *Micromachines*, 2020, **11**, 94.
35 L. Mazutis, J. Gilbert, W. L. Ung, D. A. Weitz, A. D. Griffiths and J. A. Heyman, *Nat. Protoc.*, 2013, **8**, 870–891.
36 L. Clime, K. J. Morton, X. D. Hoa and T. Veres, *Sci. Rep.*, 2015, **5**, 9765.
37 A. Kamnerdsook, E. Juntasaro, N. Khemthongcharoen, M. Chanasakulniyom, W. Sripumkhai, P. Pattamang, C. Promptmas, N. Atthi and W. Jeamsaksiri, *Colloids Interfaces*, 2023, **7**, 17.
38 K. Loizou, V. L. Wong and B. Hewakandamby, *Inventions*, 2018, **3**, 54.
39 A. Lashkaripour, C. Rodriguez, L. Ortiz and D. Densmore, *Lab Chip*, 2019, **19**, 1041–1053.
40 M. Fatehifar, A. Revell, M. Jabbari and A. De Rosis, *Phys. Fluids*, 2023, **35**, 113317.

41 H. D. Xi, H. Zheng, W. Guo, A. M. Gañán-Calvo, Y. Ai, C. W. Tsao, J. Zhou, W. Li, Y. Huang, N. T. Nguyen and S. H. Tan, *Lab Chip*, 2017, **17**, 751–771.
42 A. S. Mao, J. W. Shin, S. Utech, H. Wang, O. Uzun, W. Li, M. Cooper, Y. Hu, L. Zhang, D. A. Weitz and D. J. Mooney, *Nat. Mater.*, 2017, **16**, 236–243.
43 B. Sanchez-Correa, J. M. Bergua, C. Campos, I. Gayoso, M. J. Arcos, H. Bañas, S. Morgado, J. G. Casado, R. Solana and R. Tarazona, *Cytokine*, 2013, **61**, 885–891.
44 D. Di Carlo, D. Irimia, R. G. Tompkins and M. Toner, *Proc. Natl. Acad. Sci. U. S. A.*, 2007, **104**, 18892–18897.
45 F. Lussier, B. U. Moon, M. Janta-Polczynski, Y. Morocz, F. Svahn, M. Shen, L. Lukic, L. Malic, T. Veres, A. Ng and D. Juncker, *Adv. Mater.*, 2025, e06398.
46 M. A. A. Abdullah and J. Wang, *ACS Sens.*, 2019, **4**, 2296–2302.
47 Y. Zhou, N. Shao, R. Bessa de Castro, P. Zhang, Y. Ma, X. Liu, F. Huang, R. F. Wang and L. Qin, *Cell Rep.*, 2020, **31**, 107574.
48 F. Rey-Giraud, M. Hafner and C. H. Ries, *PLoS One*, 2012, **7**, e42656.
49 S. Chen, A. F. U. H. Saeed, Q. Liu, Q. Jiang, H. Xu, G. G. Xiao, L. Rao and Y. Duo, *Signal Transduction Targeted Ther.*, 2023, **8**, 207.
50 M. Yamada, M. Nakashima and M. Seki, *Anal. Chem.*, 2004, **76**, 5465–5471.
51 X. Lu and X. Xuan, *Anal. Chem.*, 2015, **87**, 6389–6396.
52 J. Park, S. Park, K. A. Hyun and H.-I. Jung, *Lab Chip*, 2021, **21**, 3483–3497.
53 H. Feng, A. Jafek, R. Samuel, J. Hotaling, T. G. Jenkins, K. I. Aston and B. K. Gale, *Analyst*, 2021, **146**, 3368–3377.
54 D. N. Khalil, E. L. Smith, R. J. Brentjens and J. D. Wolchok, *Nat. Rev. Clin. Oncol.*, 2016, **13**, 273–290.
55 T. T. Smith, S. B. Stephan, H. F. Moffett, L. E. Mcknight, D. Reiman, E. Bonagofski, M. E. Wohlfahrt, S. P. S. Pillai and M. T. Stephan, *Nat. Nanotechnol.*, 2018, **12**, 813–820.
56 M. Dagher, M. Kleinman, A. Ng and D. Juncker, *Nat. Nanotechnol.*, 2018, **13**, 925–932.